Journal of Materials Chemistry A

ROYAL SOCIETY OF CHEMISTRY

PAPER

View Article Online
View Journal | View Issue

Cite this: J. Mater. Chem. A, 2025, 13, 40179

3D printed barocaloric composites for environmentally friendly thermal energy management

Ignacio Delgado-Ferreiro,†[a] Ángel Ferradanes-Martínez, †[a] David González-Novo,[b] Javier García-Ben, [a] María Gelpi, [a] Jorge López-Beceiro,[c] Ramón Artiaga,[c] Julian Walker, [d] Charles James McMonagle,[e] Richard J. C. Dixey,[f] Anthony E. Phillips, [f] Sonia Zaragoza,[g] Socorro Castro-García, [a] María Antonia Señarís-Rodíguez, [a] Manuel Sánchez-Andújar, [a] Álvaro Baaliña[b] and Juan Manuel Bermúdez-García *[a]

Our society is experiencing an accelerated technological transition to reach net zero emissions by 2050, where the decarbonization of heating and cooling systems is a key aspect. In this work, we describe two new solid-state barocaloric materials, $[C_{12}H_{25}NH_3]_2MnCl_4$ and $[C_{12}H_{25}NH_3]_2MnBr_4$, with colossal barocaloric effects of $\Delta S > 200$ J K^{-1} kg^{-1}, which are already reversible under operating pressures of 500 bar. In addition, we introduce the first 3D printable barocaloric composite using a pressure transmitting matrix and thermal conductive additives, which is formed in the shape of a heat exchange gyroid. This innovative proof-of-concept demonstrates a new strategy to enhance the thermal performance, chemical stability and technological integration of the emerging family of barocaloric compounds. In addition, we identify emerging technologies (beyond traditional refrigeration) where thermal management is critical and that match the operating temperature and pressure range of the barocaloric materials obtained here, namely, lithium-ion batteries and hydrogen fuel cells.

Received 30th May 2025
Accepted 12th October 2025

DOI: 10.1039/d5ta04364f

rsc.li/materials-a

1 Introduction

The current international landscape is experiencing an accelerated technological transition towards more eco-friendly and efficient energy systems, with the objective of reaching net zero emissions by the year 2050.[1]

Lithium-ion batteries and hydrogen fuel cells are identified as two key technologies for the immediate future of cleaner energy and mobility.[2] Nevertheless, despite the significant advances that both technologies have experienced, they still present serious drawbacks concerning thermal management.[3–5] For instance, lithium-ion batteries for electric vehicles must be kept in a narrow temperature range of between 25 and 40 °C for efficient operation,[5] and thermal runaway (exothermic reactions) can be triggered by temperatures above 126 °C, posing a recognized safety risk.[6] Hydrogen fuel cells, on the other hand, can reach temperatures well over 100 °C during operation[3,4] and hydrogen storage tanks require inner pressures of up to 700 bar, where the refuelling process can also generate temperatures above 100 °C.[7] These high temperatures both accelerate the device degradation over time and decrease the energy efficiency. In both of these applications, new thermomaterials for thermal management can be used to improve the energy efficiency of high-tech devices, increase lifespan and mitigate risks associated with temperature rise.

In this context, we propose hybrid organic–inorganic perovskites as thermomaterials with great potential for use with lithium-ion batteries and hydrogen fuel cells. Hybrid perovskites already resonate in the general scientific and industrial communities as a family of advanced materials for different energy applications. In the last few years, hybrid halide perovskites have entered strongly into the race of low-cost semiconductors for efficient solar cells,[8,9] whose optoelectronic properties can be easily tuned by modifying the structural

[a]University of A Coruna, QuiMolMat Group, Department of Chemistry, Faculty of Science and Centro Interdisciplinar de Química e Bioloxía (CICA), Zapateira 15071 A, Coruña, Spain. E-mail: j.bermudez@udc.es

[b]Energy Engineering Research Group, Department of Nautical Sciences and Marine Engineering (ETSNM), University Institute of Maritime Studies, University of A Coruna, Paseo de Ronda 51 A, Coruña, 15011, Spain

[c]University of A Coruña, Ferrol Industrial Campus, CITENI-Proterm Group, 15403 Ferrol, Spain

[d]Department of Materials Science and Engineering, Norwegian University of Science and Technology, 7491 Trondheim, Norway

[e]Swiss–Norwegian Beamlines, European Synchrotron Radiation Facility, Grenoble, 38043, France

[f]School of Physics and Astronomy, Queen Mary University of London, London, E1 4NS, UK

[g]University of A Coruña (UDC), Ferrol Industrial Campus, CITENI, 15403 Ferrol A, Coruña, Spain

† These authors equally contributed to this work.

dimensionality from 3D networks down to 2D layers.[10] In the particular field of thermomaterials, 2D layered hybrid perovskites of general formula $[C_nH_{2n+1}NH_3]_2MX_4$ (n = 8–18, M = transition metal cations, X = halide anions) have been explored as promising materials for thermal management since the late 1970s.[11,12] These compounds present $[C_nH_{2n+1}N]^+$ long-chain alkylammonium cations placed between layers of $[MX_6]$ octahedra in a sandwich-like structure. The degrees of freedom of the alkylammonium chains, together with their weak interactions with the metal halide octahedral layers, allow the molecular cation sub-lattice to reach a molten-like state above a critical temperature, while the rigid octahedral network allows the compound to remain in the solid state. These thermally-induced solid–solid phase transitions produce very large thermodynamic changes and tunable transition temperature as a function of the *n*-value, which are of great interest for passive thermal energy storage applications.[11]

Even more recently, this family of 2D layered perovskites was revisited for active barocaloric refrigeration and heating applications. Specifically, $[C_{10}H_{21}NH_3]_2MnCl_4$, $[C_9H_{19}NH_3]_2MnCl_4$ and $[C_9H_{19}NH_3]_2CuCl_4$ were found to exhibit very large thermal changes (barocaloric effects) related to pressure-induced solid–solid phase transitions,[13–15] superior to most of the reported barocaloric materials to date.

In the last decade, barocaloric materials have emerged as promising solid-state thermomaterials for eco-friendly refrigeration, heating and energy storage in thermal batteries.[16,17] Over the years, different families of barocaloric compounds have been explored, including metallic alloys, inorganic ammonium and phosphate salts,[18–26] plastic crystals,[27–35] polymers,[36–38] superionic conductors,[39,40] spin crossover compounds,[41–47] hybrid organic-inorganic perovskites[13–15,48–52] and even MOFs.[53,54]

Despite this scientific interest and many breakthroughs, few barocaloric compounds have thus far been implemented in real applications.[55] There are still critical limitations to overcome before reaching the market. Traditional refrigeration systems (*i.e.* fridges and/or air-conditioners) operate below 30 bar and at ambient temperature. Meanwhile, most barocalorics operate well above 1000 bar and at temperatures higher than room temperature, often >60 °C.[56] Therefore, it is necessary to decrease the operating temperature and pressure ranges and/or identify new applications that match these operating conditions. In addition, barocaloric materials generally exhibit very low thermal conductivity, which hinders heat transfer from and/or towards the heat exchangers of a given device. The addition of carbon conductive powders dispersed as fillers within the barocaloric materials has emerged as one approach for overcoming the challenge of low thermal conductivity.[14,57,58]

Another general concern when designing barocaloric technologies is how to integrate the barocaloric materials into devices. These compounds are often obtained in the form of brittle powders that will have to be suspended or in contact with heat exchange or pressurization fluids within a given device. Here, they pose a risk of diffusing along the device pipes and creating undesired clogs. However, if this risk is eliminated by shaping the barocaloric material into a more compact solid (*i.e.* bulky pellets), the surface area in contact with the heat transfer fluid will be too low for efficient heat exchange. To overcome this challenge, new and innovative ways of integrating barocaloric materials into thermal devices are needed.

In this work, our main goal is to expand the portfolio of available barocaloric materials and, even more, to provide innovative materials engineering solutions that could accelerate the technological implementation of barocaloric materials, presenting the first examples of cast and 3D printed barocaloric composites.

In that regard, we present two new members of the emerging family of barocaloric 2D hybrid perovskites, specifically the $[C_{12}H_{25}NH_3]_2MnCl_4$ and $[C_{12}H_{25}NH_3]_2MnBr_4$ compounds. These thermomaterials exhibit thermal changes as large as ΔS ~200 J K^{-1} kg^{-1} that can be reversibly driven in a temperature range of 315–350 K (42–77 °C) and under pressures of 500–700 bar. Accordingly, we identify that the operating conditions of $[C_{12}H_{25}NH_3]_2MnCl_4$ and $[C_{12}H_{25}NH_3]_2MnBr_4$ – well above room temperature – are of interest for avoiding overheating and/or thermal runaway of Li-ion batteries and hydrogen fuel cells and storage tanks, opening new thermal management opportunities for these emerging technologies.

In addition, we also develop barocaloric composites that can enhance chemical protection, thermal conductivity and heat transfer surface, using polymeric matrices that can adopt any shape by *in situ* co-polymerization and also by 3D printing. These composites incorporate the active barocaloric material and graphite as an additive to enhance the thermal conductivity. Furthermore, we are able to develop a first proof-of-concept of a 3D printed heat exchanger that will increase the surface area in contact between the barocaloric composite and a given heat transfer fluid.

2 Results and discussion

2.1 Barocaloric properties of the $[C_{12}H_{25}NH_3]_2MnCl_4$ and $[C_{12}H_{25}NH_3]_2MnBr_4$ compounds

The $[C_{12}H_{25}NH_3]_2MnCl_4$ and $[C_{12}H_{25}NH_3]_2MnBr_4$ compounds were obtained as pure polycrystalline powders, as confirmed by powder X-ray diffraction (PXRD), see Fig. S1 of the SI. These materials show a PXRD pattern similar to that of the simulated pattern from the single-crystal structure reported for the $[C_{12}H_{25}NH_3]_2MnCl_4$ compound (Fig. S1 of the SI).[12] It should be noted that, even if the chloride analogue has been widely studied,[59–63] single-crystal data have just been recently reported.[12] The bromide-containing compound $[C_{12}H_{25}NH_3]_2MnBr_4$—to the best of our knowledge—is reported for the first time in the present work.

According to our variable-temperature differential scanning calorimetry (VT-DSC) curves at ambient pressure, both compounds exhibit a wide thermal peak at ~328 K on heating and at 322 K on cooling. In the particular case of the Cl-compound, DSC data suggest an overlap of two consecutive transitions, as evidenced by the small shoulder observed during the cooling process (see Fig. S2 of the SI). This is in agreement with the literature, where 2 solid–solid phase transitions are observed at very close temperatures for $[C_{12}H_{25}NH_3]_2MnCl_4$.[59]

As can be observed in Fig. 1, both Cl- and Br-compounds exhibit a similar behaviour with a small thermal hysteresis of ~6 K, and thermal changes of ΔH ~83 kJ kg^{-1} and ΔS ~255 J K^{-1} kg^{-1}. Therefore, the anion seems to have an almost negligible effect on the thermodynamic parameters at ambient pressure.

The barocaloric performance of these compounds was evaluated by quasi-direct and direct methods using high-pressure differential scanning calorimetry, as reported elsewhere.[16] For the quasi-direct methods, we performed VT-DSC analysis under different isobaric conditions (see Fig. 1).

In both compounds, the phase transition is shifted towards higher temperatures upon pressurization (Fig. 1a and b), with similar barocaloric coefficients of dT_t/dp ~17 K kbar^{-1} (Fig. 1c and d), which is in the same range as reported for barocaloric 2D hybrid perovskites.[13–15]

The barocaloric effect in terms of isothermal entropy change (ΔS) was calculated by quasi-direct methods considering the additional entropy changes, as described in the Methods section. Fig. 1e and f show that both Cl- and Br-compounds already exhibit reversible barocaloric effects of ΔS_{rev} ~ 200 J K^{-1} kg^{-1} at 700 bar, which can increase up to ΔS_{rev} ~ 230 J K^{-1} kg^{-1} at the maximum applied pressure.

In order to confirm the barocaloric effects estimated by quasi-direct methods, we also performed direct observations of the thermal changes obtained during application and removal of pressure under different isothermal conditions using variable-pressure differential scanning calorimetry, VP-DSC (Fig. 2). These analyses confirm that the barocaloric effects can be reversibly driven already under pressures of ~500 bar.

In addition, the peak integration reveals barocaloric effects as large as ΔS_{direct} ~ 270 J K^{-1} kg^{-1}, which are slightly larger than those calculated by quasi-direct methods. It should be noted that these barocaloric effects are similar to those of the analogue $[C_{10}H_{21}NH_3]_2MnCl_4$ compound, which range within the largest barocaloric effects reported to date.[13,15]

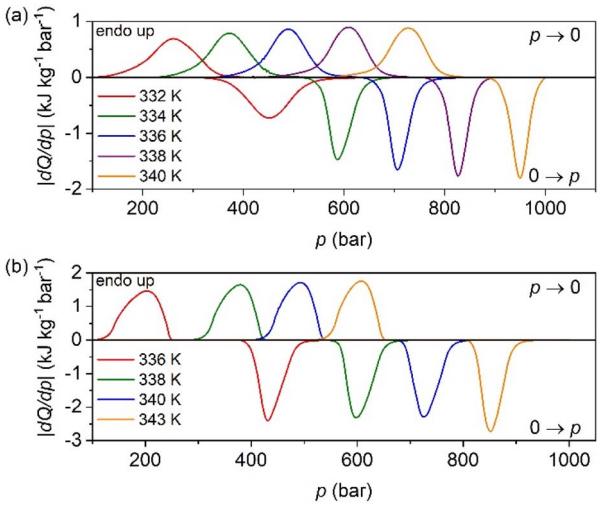

Fig. 2 VP-DSC curves of heat flow, dQ/dp, *versus* directly applied pressure, p, for the (a) $[C_{12}H_{25}NH_3]_2MnCl_4$ and (b) $[C_{12}H_{25}NH_3]_2MnBr_4$ compounds. Note: endothermic curves are plotted upwards.

These findings suggest that neither the substitution of Cl^- by Br^- nor the chain-size increase from $n = 10$ (ref. 13) to $n = 12$ (this article) seems to significantly affect the thermal changes. Nevertheless, this modification in the chain largely shifts the transition temperature from ~310 K ($n = 10$) to ~330 K ($n = 12$), which makes our materials more suitable for higher temperature applications.

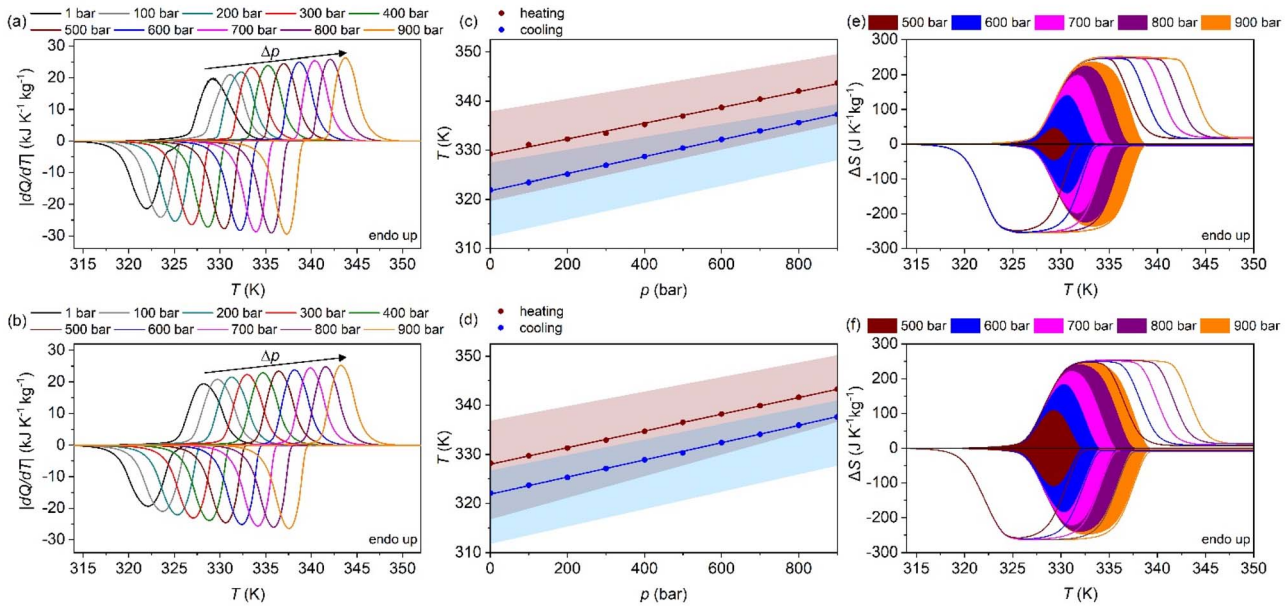

Fig. 1 (a and b) VT-DSC curves at different pressures, (c and d) T–p phase diagrams, and (e and f) reversible barocaloric effects for $[C_{12}H_{25}NH_3]_2MnCl_4$ (top) and $[C_{12}H_{25}NH_3]_2MnBr_4$ (bottom), respectively. Note: solid lines and dots in the T–p diagrams are taken from the maximum of the peaks, while the shaded areas represent the peak widths.

2.2 Structural origin of the barocaloric effects of the $[C_{12}H_{25}NH_3]_2MnCl_4$ and $[C_{12}H_{25}NH_3]_2MnBr_4$ compounds

In order to delve into the nature of the observed phase transitions and barocaloric effects, we carried out variable-temperature and variable-pressure synchrotron powder X-ray diffraction (SPXRD) experiments for both compounds.

In the case of VT-SPXRD (Fig. 3a and b), we observe a drastic structural change at $T \sim 330$ K associated with a first-order transition between two different polymorphs, a result which is in agreement with the thermal transition observed by VT-DSC.

It is worth noting that there is a short temperature range close to the phase transition temperature where both phases coexist, indicating that the phase transition occurs in two steps. This observation aligns with the broad peaks observed in the DSC curves.

Very interestingly, the VP-SPXRD patterns (Fig. 3e and f) clearly reveal a new and intermediate phase between the high-temperature (HT) PI phase and low-temperature (LT) PII phase crystal structures previously observed in VT-SPXRD at atmospheric pressure.

Using these SPXRD data, we have been able to perform Le Bail refinements of the three different phases (Fig. S3 of the SI). Here, the HT phase I was successfully fitted to an orthorhombic *Cccm* space group with lattice parameters of $a\sim$ 7.31 Å, $b\sim$ 7.33 Å, $c\sim$ 66.4 Å. Meanwhile, the LT phase II was fitted to a triclinic $P\bar{1}$ group, where $a \sim 5.08$ Å, $b \sim 5.11$ Å, $c\sim$ 30.1 Å, $\alpha \sim 91.2°$, $\beta \sim 92.5°$ and $\gamma\sim 90.6°$. It should be noted that this latter phase is in agreement with the recently reported single-crystal XRD data.[12]

The evolution of the lattice parameters with temperature at ambient pressure is shown in Fig. S4 of the SI. Both materials exhibit volume changes of $\Delta v\sim$ 8.4% (Fig. 3c and d), and expansion coefficients of 2.3×10^{-4} K^{-1} (Cl-compound) and 3.8×10^{-4} K^{-1} (Br-compound), values that are similar to the $n = 10$ analogue compound.[14]

Regarding the metastable intermediate phase, we found that it exhibits a monoclinic symmetry with $P2_1/a$ space group with $a\sim$ 7.27 Å, $b\sim$ 7.33 Å, $c\sim$ 66 Å and $\beta \sim 95°$ (see Le Bail refinements, Fig. S5 of the SI). Fig. 3(g and h) shows a volume decrease upon pressurization with two abrupt transitions, which exhibit volume changes of ~2.2% and 6.0%, respectively. It should be noted that these volume changes of the two well-resolved transitions are equivalent to the total volume change when undergoing directly from phase II to phase I (Δv ~8.4%).

In addition, using the Birch–Murnaghan equations, we found that these materials exhibit an isothermal bulk modulus of B_0 ~4.21(4) MPa and B_0 ~5.31(5) MPa for the Cl- and Br-compounds, respectively.

Similarly to the barocaloric $[C_{10}H_{21}NH_3]_2MnCl_4$, $[C_9H_{19}NH_3]_2MnCl_4$ and $[C_9H_{19}NH_3]_2CuCl_4$ compounds,[13–15] the barocaloric effects in the materials described here can be attributed to order–disorder transitions where the conformation of the alkylammonium chain is modified, as supported by the recent literature.[12,63]

In this context, it has been reported that the conformational and volumetric entropy are the terms that play a major role in the phase transitions for 2D layered perovskites with long-chain alkylammonium cations.[14] Accordingly, the volumetric entropy term, ΔS_v, describes the entropy change resulting from volume expansion without considering any associated disordering processes. We can calculate this term as $\Delta S_v = (\alpha\, B_o)\cdot\Delta v$, where α, B_o, and Δv denote the isobaric thermal expansibility, bulk modulus, and the specific volume change of the transition at ambient pressure, respectively. The obtained value of ΔS_v is ~72 and ~80 J K^{-1} kg^{-1} for the Cl- and Br-compounds, respectively. Therefore, the contribution of ΔS_v to the total transition entropy is relatively low, of around 31–35%, which is slightly lower than for similar layered perovskites.[14]

In the case of the conformational disordering of the dodecylammonium chain from an all-trans configuration, the associated entropy change can be estimated as $\Delta S_c = R \ln 3^{n-2} =$ 91.29 J K^{-1} mol^{-1} (~160 J K^{-1} kg^{-1} and ~122 J K^{-1} kg^{-1} for the

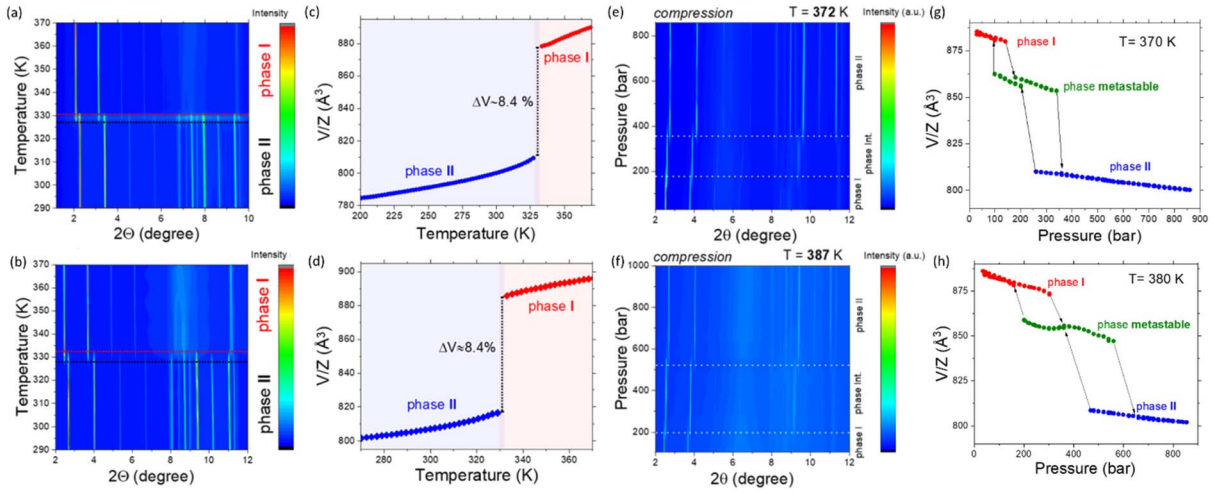

Fig. 3 (a and b) Contour plots of VT-SPXRD patterns and (c and d) evolution of the volume cell as a function of temperature for the $[C_{12}H_{25}NH_3]_2MnCl_4$ (top) and $[C_{12}H_{25}NH_3]_2MnBr_4$ (bottom) compounds. Note: dashed lines represent a region of coexistence of phases I and II. (e and f) Contour plot of VP-SPXRD patterns and (g and h) evolution of the volume cell as a function of pressure at different temperatures for $[C_{12}H_{25}NH_3]_2MnCl_4$ compounds.

Cl- and Br-analogues), being a major contribution to the total entropy change of the transition.

Therefore, it can be concluded that the origin of the barocaloric effects in $[C_{12}H_{25}NH_3]_2MnCl_4$ and $[C_{12}H_{25}NH_3]_2MnBr_4$ can be mainly attributed to configurational disorder.

2.3 Barocaloric composites of $[C_{12}H_{25}NH_3]_2MnCl_4$ embedded in polymeric matrices with thermal conductive additives

In order to propose innovative alternatives to facilitate conformation and protection of barocaloric materials, as well as to maximize their heat transfer surface and enhance their thermal conductivity, we have developed two different composites. Each composite is based on a different polymer matrix: the commercial Sylgard 184 (based on polydimethylsiloxane, PDMS) and the 3D printing F39 resin (based on a mixture of acrylated aliphatic urethane, 4-acryloylmorpholine and diphenyl(2,4,6-trimethylbenzoyl)-phosphine oxide). In addition, we have also incorporated graphite powders to enhance the thermal conductivity.

In that regard, we have been able to fabricate composites of Sylgard 184 with a maximum load of ~19% (w/w) of the barocaloric $[C_{12}H_{25}NH_3]_2MnCl_4$ material and ~7% (w/w) of graphite powder. Meanwhile, the 3D printed composites of F39 resin incorporate a maximum load of ~16% (w/w) of $[C_{12}H_{25}NH_3]_2MnCl_4$ and ~5.5% (w/w) of graphite powders. Powder XRD data confirm the presence of $[C_{12}H_{25}NH_3]_2MnCl_4$ in the respective polymeric matrices (see Fig. S6 and S7 of the SI). Meanwhile, EDX analysis shows a homogeneous distribution of the $[C_{12}H_{25}NH_3]_2MnCl_4$ particles in both polymeric matrices (see Fig. S8 and S9 of the SI).

Moreover, in both cases, we have been able to increase the thermal conductivity from 0.2 to 0.3 W m^{-1} K^{-1} for the final composites (see Fig. S10 and S11 of the SI). This increase is similar to those observed in recently reported barocaloric composites formed just by adding graphite and/or graphene additives, such as $[C_{10}H_{21}NH_3]_2MnCl_4$(80%):graphite(20%)[14] with an increase from ~0.2 to 0.35 W m^{-1} K^{-1}; PDMS(80%):-graphite(20%) with an increase from 0.16 W m^{-1} K^{-1} to 0.37 W m^{-1} K^{-1};[58] or NPG-TMP(95%):graphene(5%) (NPG: neopenthylglicol; TMP: trimethylolpropane)[64] with an increase from 0.19 to 0.4 W m^{-1} K^{-1}. Advantageously, we reach similar values with lower loads of graphite and, even more relevant, we have been able to shape the barocaloric composites at will, so the heat exchange surface can be enhanced for much faster heat transfer, as later discussed. For instance, in the case of Sylgard 184 composites, we have fabricated cylindrical pellets by direct co-polymerization curing using a template (Fig. 4a). Meanwhile, for the F39 resin, we have been able to 3D print not only cylindrical pellets but also complex gyroid structures that contain the barocaloric material and maximize the heat transfer surface, which serves as a proof-of-concept for future 3D printed barocaloric heat exchangers (Fig. 4b).

VT-DSC analysis at ambient pressure (see Fig. 4c) enabled the calculation of the effective load of the barocaloric $[C_{12}H_{25}NH_3]_2MnCl_4$ compound in the final composites as the ratio of

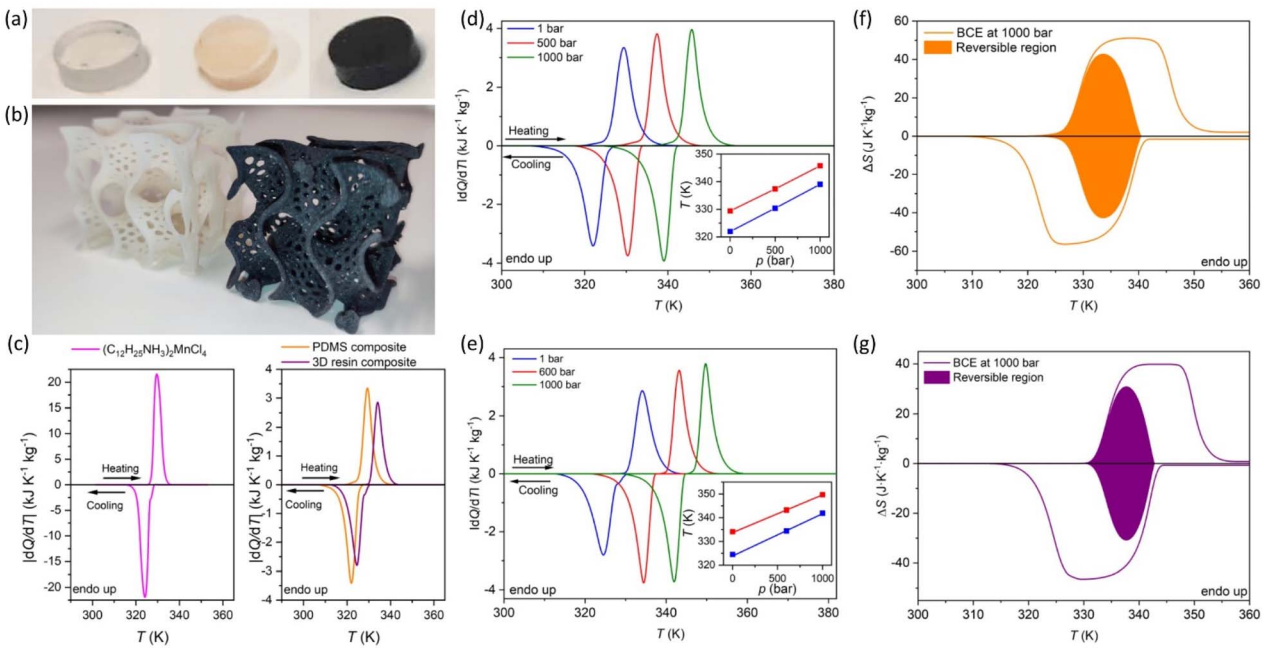

Fig. 4 (a) Composite pellets of Sylgard 184: pure (left), embedded with 19% (w/w) of $[C_{12}H_{25}NH_3]_2MnCl_4$ (middle) and embedded with 19% (w/w) of $[C_{12}H_{25}NH_3]_2MnCl_4$ and 7% of graphite powders. (b) 3D printed gyroid structure of F39 resin embedded with 16% (w/w) of $[C_{12}H_{25}NH_3]_2MnCl_4$ (left), and with 16% (w/w) of $[C_{12}H_{25}NH_3]_2MnCl_4$ and 5.5% (w/w) of graphite powders. (c) VT-DSC curves at ambient pressure for the $[C_{12}H_{25}NH_3]_2MnCl_4$ pure material compared with the Sylgard 184 and F39 composites. (d and e) VT-DSC curves at different pressures for the Sylgard 184 (PDMS) and F39 (3D resin) composites, respectively. (f and g) Barocaloric effects (BCE) in terms of isothermal entropy changes (ΔS) for the Sylgard 184 and F39 composites.

the enthalpy change of the composites ($\Delta H_{composite}$) divided by the enthalpy change of the pure barocaloric material ($\Delta H_{barocaloric}$), *i.e.* $\text{load}(\%) = \left(\frac{\Delta H_{composite}}{\Delta H_{barocaloric}}\right) \times 100$, where the observed loads for the Sylgard 184 and F39 composites are 19.0% (w/w) and 16.1% (w/w), respectively. These values are indicative of the total thermal response attainable for both composites.

Remarkably, the composites retain the thermal transition of the pure barocaloric material, with transition temperatures at ~328 K on heating and similar thermal hysteresis of ~7 K. In turn, we have also analysed the pressure response and barocaloric properties of the obtained composites by quasi-direct (VT-DSC at different pressures) and direct (VP-DSC at different temperatures) measurements. Similar to the pure barocaloric material, in the obtained composites the phase transition shifts towards higher temperatures when applying pressure from 1 to 1000 bar, displaying barocaloric coefficients of $dT_t/dp \sim 17$ K kbar^{-1} (Fig. 4d and e), in perfect agreement with the coefficient observed for the pure $[C_{12}H_{25}NH_3]_2MnCl_4$ material.

This significant finding highlights that the polymeric matrices with graphite additives do not hinder the pressure transmission towards the barocaloric $[C_{12}H_{25}NH_3]_2MnCl_4$ material. Therefore, these matrices are suitable media to encapsulate barocaloric materials without affecting their pressure responsiveness.

In addition, we have also calculated the isothermal entropy changes by quasi-direct methods (as described in the Methods section), obtaining reversible barocaloric effects as large as $\Delta S_{rev(Sylgard\ 184)} \sim 40.2$ J K^{-1} kg^{-1} and $\Delta S_{rev(F39)} \sim 30.9$ J K^{-1} kg^{-1} under pressurization of 1000 bar (see Fig. 4f and g). The composite with F39 resin exhibits a lower value for ΔS_{rev}, attributed to a slightly larger thermal hysteresis.

An important practical aspect of the composite materials is the mechanical behavior in comparison with pure barocaloric materials. The mechanical properties were therefore studied by dynamic mechanical analysis (DMA). As can be observed in Fig. 5, the compressibility of the PDMS and 3D printed composites increases in comparison with the pure $[C_{12}H_{25}NH_3]_2MnCl_4$ barocaloric material (in the shape of a cold-press pellet). This is directly related to the significantly large compressibility of the starting polymers (F39 and PDMS), which is noticeably larger in the case of PDMS. In any case, this elastic behavior in both polymorphs facilitates the hydrostatic compression of the $[C_{12}H_{25}NH_3]_2MnCl_4$ particles embedded in the polymeric matrices. Moreover, for further assessment of the mechanical robustness and stability of these composites, we have performed over 100 pressurization cycles over time at a rate of 40 bar min^{-1} in the 3D printed pellet samples (see Fig. S12), which maintained the barocaloric response for over 80 hours. Additionally, in order to test the mechanical robustness of the gyroid-like structure, we run 100 pressurization cycles (over a small fragment due to space limitations of the sample holder) under a much faster pressurization rate (115 bar-min^{-1}), which revealed that the tested sample maintain the original shape of the gyroid fragment (see Fig. S13). In the same

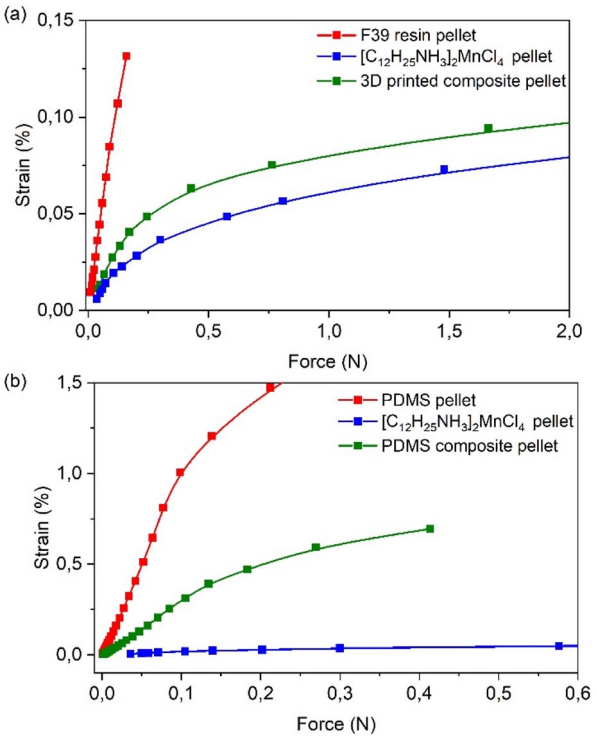

Fig. 5 Strain *versus* force compression curves for the different polymeric matrices and composites of F39 (a) and PDMS (b) in comparison with the $[C_{12}H_{25}NH_3]_2MnCl_4$ barocaloric material.

line, thermogrametric analysis reveals that these composites offer a thermal stability up to ~250 °C (see Fig. S14), similar to the pure barocaloric material and in agreement with similar reported 2D-layered perovskites.[14]

In order to perform an initial evaluation of additional parameters on the 3D printed composites, we have observed that the concentration of the additives ($[C_{12}H_{25}NH_3]_2MnCl_4$ and graphite) is critical and directly affects their thermal properties. When increasing the ratio of $[C_{12}H_{25}NH_3]_2MnCl_4$ from ~6% (w/w) to ~30% (w/w), we are able to increase the thermal response of the material, see Fig. S15. Nevertheless, for concentrations larger than 30% (w/w), material agglomerations appear, hindering 3D printing, see Fig. S16. In addition, we observe that the graphite ratio is also very critical, since concentrations larger than ~5.5% (w/w) absorb too much UV light from the printer, and the composite cannot be printed. Actually, when using graphite as an additive for 3D printing, the exposure time per layer had to be increased from 35 seconds to 250 seconds. Furthermore, when adding 5.5% (w/w) graphite, we can only add ~16% (w/w) of active material before clogs start to appear. In any case, we anticipate that using different light sources and adding dispersants could allow an increase in the graphite and thermomaterial loading in the composites.

It should be noted that even if we are using only ~16% (w/w) of active barocaloric material in each composite, we still observe very large thermal changes similar to and even superior to other pure barocaloric materials such as $(NH_4)_2SO_4$,[19] or [TPrA][Mn(dca)$_3$].[48] Furthermore, these composites offer the

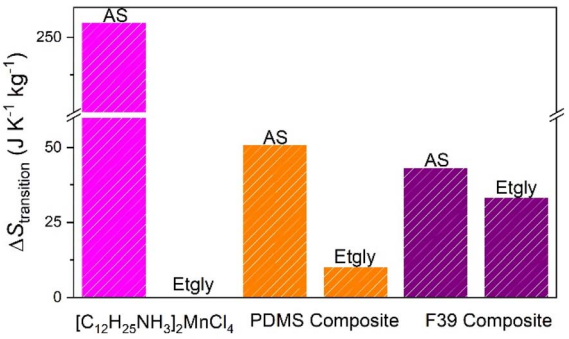

Fig. 6 Comparison of the thermal performance (in terms of entropy changes) of the as-synthesized (AS) samples and the same samples after 3 days in ethylene glycol (Etgly) under magnetic stirring.

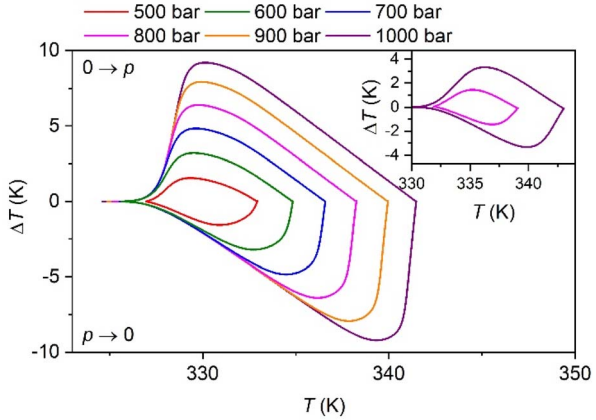

Fig. 7 Reversible adiabatic temperature changes calculated by quasi-direct methods on applying ($0 \rightarrow p$) and removing ($p \rightarrow 0$) pressure for the $[C_{12}H_{25}NH_3]_2MnCl_4$ pure material and the 3D printed composite (inset).

advantage of easy conformation, chemical protection against fluids and enhanced heat transfer with the incorporation of thermal conductive additives, such as graphite. Fig. 6 shows the chemical stability of pure $[C_{12}H_{25}NH_3]_2MnCl_4$ and of the PDMS and F39 (3D printed) composites after 3 days in a commonly used heat transfer fluid, namely, ethylene glycol.

The stability studies compare the entropy change (in relative percentage) of the as-synthesized samples (labelled as AS) in comparison with the entropy changes after three days in ethylene glycol (labelled as Etgly) under magnetic stirring. In the case of the as-synthesized $[C_{12}H_{25}NH_3]_2MnCl_4$ compound, we observe that it completely dissolves after a few minutes. Therefore, this material is not chemically stable in ethylene glycol, a very common heat exchange fluid. Meanwhile, the PDMS and F39 (3D printed) composites retain up to 20 and 80% of the thermal response, respectively, as observed by DSC (see Fig. S17 and S18 of the SI), which increases the chemical stability of the barocaloric compound. We observe that the F39 resin offers better protection against heat exchange fluids.

2.4 Heat exchange in $[C_{12}H_{25}NH_3]_2MnCl_4$ and its 3D composite

In order to further evaluate the impact of composites modelling on the barocaloric materials, we have analysed the adiabatic temperature change in the pure $[C_{12}H_{25}NH_3]_2MnCl_4$ material and in the 3D printed composite, and we have also performed heat exchange simulations to evaluate the thermalization over time.

The adiabatic temperature change has thus been calculated from quasi-direct methods for both the pure $[C_{12}H_{25}NH_3]_2MnCl_4$ barocaloric material and the 3D printed composite, as reported in the literature (eqn (1)), see Fig. 7:

$$|\Delta T(S; p_{atm} \leftrightarrow p)| = |T(S; p) - T(S; p_{atm})|\Delta T = -(T/C_p)\Delta S_{it} \quad (1)$$

As can be observed, the pure $[C_{12}H_{25}NH_3]_2MnCl_4$ barocaloric material can reach values as large as $\Delta T \sim 9$ K under pressurization of 1000 bar, similar to other colossal barocaloric materials.[15,65] Meanwhile the 3D printed composites reaches lower values of only $\Delta T \sim 3.3$ K. Of course, these values could be improved by increasing the loading of the barocaloric material in the composite.

In contrast, regarding the heat exchange, we have considered different scenarios, namely (1) thermalization by natural air convection and (2) thermalization by fluid flow of ethylene glycol (a common heat exchange fluid).

In the first scenario of natural convection, a compact cube of pure $[C_{12}H_{25}NH_3]_2MnCl_4$ and a gyroid cube of the F39 composite, both with the same mass, are compared. These cubes are left to thermalize from 70 °C (temperature slightly above the barocaloric transition) down to ambient temperature. As can be observed in Fig. 8 and 9, the gyroid 3D printed composite fully thermalizes down to room temperature in 5–10 minutes. Meanwhile, the pure $[C_{12}H_{25}NH_3]_2MnCl_4$ material needs over 30 minutes to reach ambient temperature.

In the second scenario, we consider the same cubes inside a cylindrical pipe where a heat exchanger fluid (ethylene glycol) is flowing (Fig. 10).

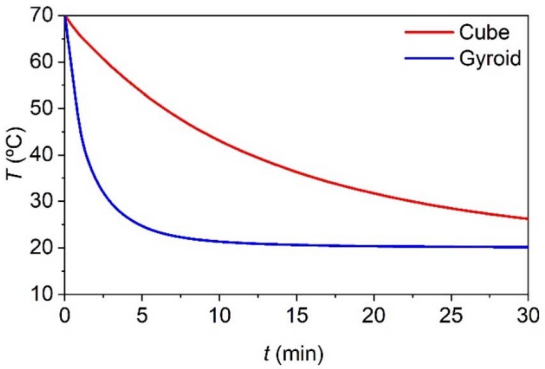

Fig. 8 Simulated data of thermalization by natural air convection over time for the pure $[C_{12}H_{25}NH_3]_2MnCl_4$ material in comparison with a 3D printed composite in the shape of a gyroid structure.

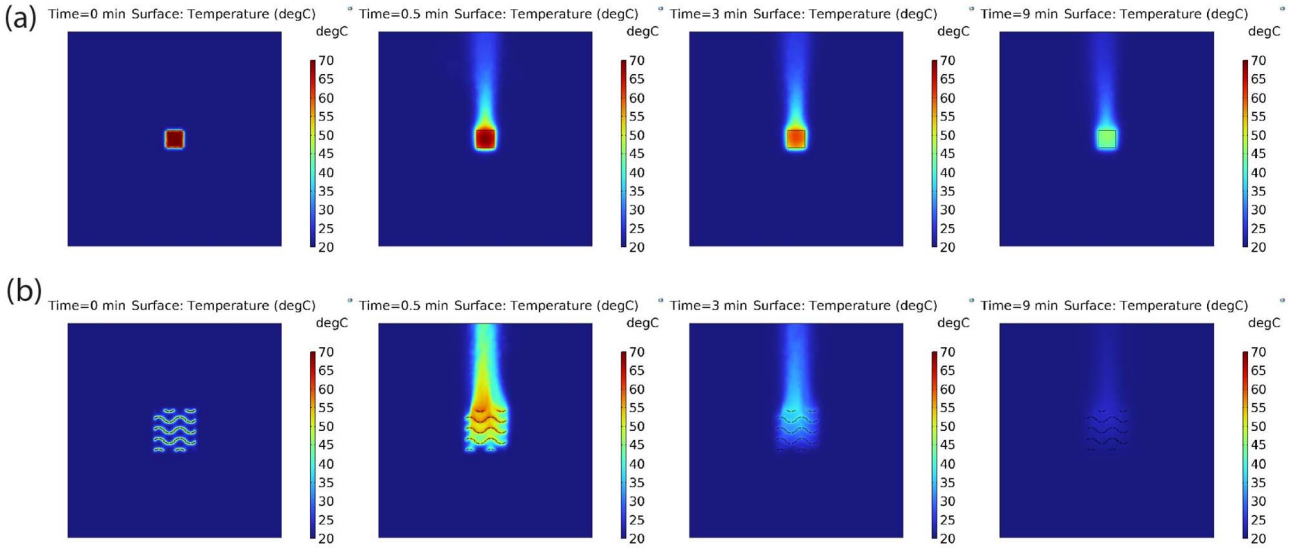

Fig. 9 Simulated heat transfer by natural convection in the cross section of a cube of (a) $[C_{12}H_{25}NH_3]_2MnCl_4$ and (b) a gyroid-cube of the $[C_{12}H_{25}NH_3]_2MnCl_4$ composite printed in 3D resin, representing thermalization over time in a period of 0, 0.5, 3 and 9 min from left to right.

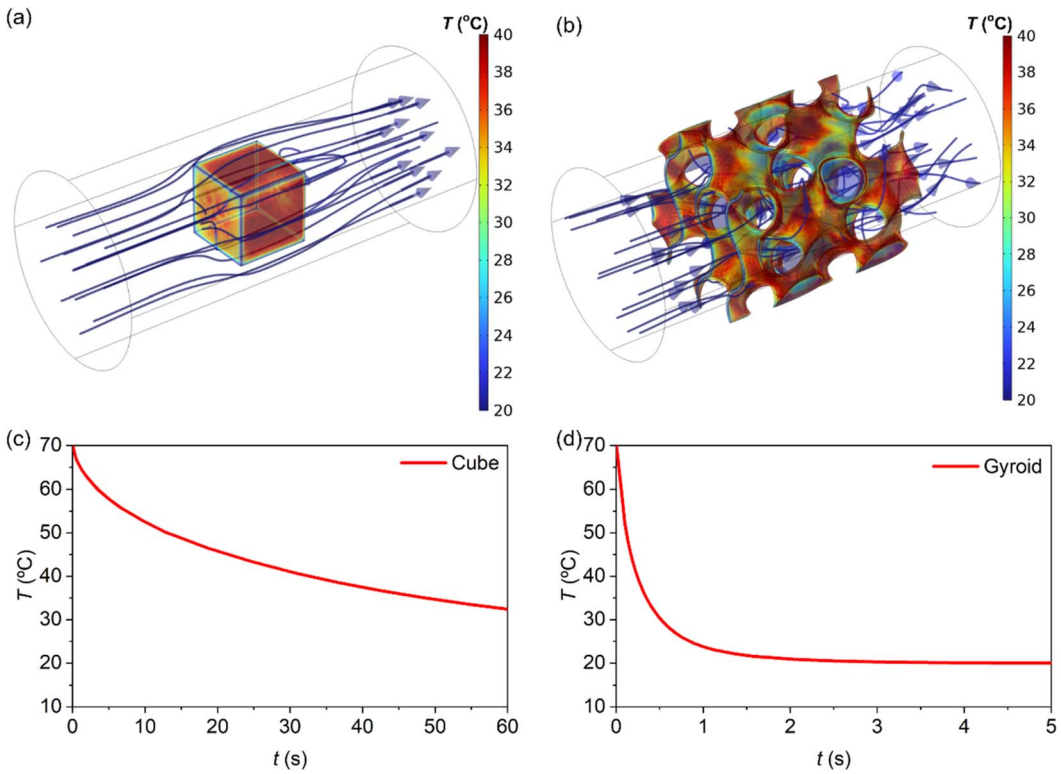

Fig. 10 (a and b) Simulated flow lines of ethylene glycol around the $[C_{12}H_{25}NH_3]_2MnCl_4$ cube and the 3D printed gyroid composite inside a pipe, respectively. (c and d) Simulated thermalization profile over time for the $[C_{12}H_{25}NH_3]_2MnCl_4$ cube and the 3D printed gyroid composite in ethylene glycol, respectively.

In this case of "forced" thermalization, both samples fully thermalize in a matter of seconds. Nevertheless, there is still an important time difference between the $[C_{12}H_{25}NH_3]_2MnCl_4$ pure material and the 3D printed composite (see Fig. 10). While the pure material needs over 60 seconds to reach ambient temperature, the 3D printed composite reaches room temperature in only 2 seconds. Moreover, it is worth remembering that the pure material is not stable in ethylene glycol, as experimentally observed in this work (Fig. 6).

2.5 Outlook

The family of barocaloric 2D hybrid organic–inorganic perovskites represents a class of materials with great potential for thermal management applications, not only for passive thermal energy storage as proposed since the 1970s, but also for active barocaloric cooling and heating applications. The transition temperature of these compounds can be easily tuned by the modification of the alkylammonium chain, as observed in this work and in previous barocaloric studies.[13–15]

In the case of the $[C_{12}H_{25}NH_3]_2MnCl_4$ and $[C_{12}H_{25}NH_3]_2MnBr_4$ compounds presented here, their relatively high transition temperature at ~330 K put into the spotlight new potential applications above room temperature for barocaloric materials, which have been not discussed to date, namely thermal management of lithium-ion batteries and hydrogen fuel cells and storage tanks,[3–5] different from their more traditional application in fridges, air-conditioners and/or heat-pumps.

To date, the main limitations of barocaloric materials that prevent technological applications are the relatively high operating pressures ($p > 1000$ bar) and, in most cases, relatively high operating temperatures ($T > 330$ K).

In this regard, these materials could find applications in technologies operating above room temperature, such as refrigerating lithium-ion batteries and/or hydrogen fuel systems to keep them below 373 K, which are critical temperatures for thermal runaway (in the case of lithium batteries),[6] and are easily reached in the case of hydrogen fuel cells and storing tanks during operation[3,4] and/or refueling.[7] In addition, the hydrogen systems already operate under pressures of over 700 bar, so the relative operating pressures of most barocaloric materials would not be a limitation, contrary to traditional fridges or air conditioners, where the operating pressure is generally below 30 bar. It should be highlighted that there are already circulating vehicles combining both pressurized hydrogen systems and Li-ion batteries,[66] which could benefit from barocaloric thermal management. For instance, the inner walls of hydrogen storage tanks could be covered with barocaloric materials (conventional and/or inverse) following similar strategies to those proposed for phase change materials for thermal energy storage.[67,68] Similarly, barocaloric materials could be used to recover mechanical energy from pressurized hydrogen systems and/or compressors—a topic of increasing interest—[69,70] and turn it into heating and/or cooling power, where non-pressurized secondary heat transfer fluids could safely transfer the heat from/towards a barocaloric core.[71]

Therefore, these two innovative applications must be considered when designing new barocaloric materials and/or technologies in the future, including life cycle assessments and cost-benefit aspects in comparison with other alternative solutions.

In addition, future studies need to consider new conformation strategies for protecting barocaloric materials and adapting them to specific geometric constrictions during device integration. In this work, we present the first proof-of-concept demonstrating that barocaloric materials can be successfully integrated and protected in flexible polymeric matrices without affecting their pressure responsiveness. These composites can be shaped and conformed at will, even in very complex structures simulating heat exchangers (*i.e.* gyroid-type structures), by direct co-polymerization and even by 3D printing techniques. These barocaloric composites can offer chemical protection against heat exchange fluids (*i.e.* ethylene glycol) while exhibiting a good thermal and mechanical stability, although the load capacity of barocaloric materials and thermal conductive additives is still limited, especially for photo-cured 3D printing, where a trade-off between adequate viscosity and UV-light adsorption by additives (*i.e.* graphite) must be considered.

These findings open a new path for the barocaloric community towards a closer technological implementation, where future studies must address key aspects such as load maximization, shape optimization, heat exchange simulations, and/or long-term stability, among others.

3 Conclusions

This work presents two new members of barocaloric 2D hybrid organic–inorganic perovskites, specifically, the $[C_{12}H_{25}NH_3]_2MnCl_4$ and $[C_{12}H_{25}NH_3]_2MnBr_4$ compounds. These compounds exhibit colossal barocaloric effects of $\Delta S > 200$ J K^{-1} kg^{-1}, already reversible under pressures of 500 bar, while operating at relatively high temperatures of >330 K. These technical specifications could be suitable to integrate these materials in thermal management systems for two innovative technologies, namely lithium-ion batteries and hydrogen fuel cells and storage tanks. These technologies can reach temperatures of above 373 K, while hydrogen systems operate under pressures of over 700 bar. Therefore, these technologies could benefit from this type of barocaloric material, while the operating conditions of temperature and/or pressure are similar to those required for the barocaloric materials reported here.

It is also observed that, although the entropy changes are not affected by the substitution of Cl^- for Br^- nor by the increase in the chain size from $n = 10$ to $n = 12$, the temperature at which the transition occurs is markedly affected. This indicates a possible path for customized tuning of the properties depending on the requirements.

In addition, we also present new conformation techniques by fabricating two barocaloric composites of $[C_{12}H_{25}NH_3]_2MnCl_4$ embedded in flexible polymeric matrices of Sylgard 184 and of F39 3D printed resin, combined with a thermal conductive graphite additive. Remarkably, these composites can be shaped at will by direct co-polymerization (Sylgard 184) and even by simple 3D printing (F39 resin). Actually, we have demonstrated, as a first proof-of-concept, that barocaloric composites can be 3D printed in complex gyroid structures simulating heat exchanges for maximizing the heat transfer surface. Even more, our stability studies and our heat transfer simulations already highlight the advantages of using barocaloric 3D printed composites in comparison with the pure barocaloric materials.

Therefore, these findings not only expand the family of barocaloric 2D hybrid perovskites with two new members, but also identify new potential applications for advanced

technologies, and demonstrate innovative conformation techniques for developing future 3D printed barocaloric heat exchangers towards future technological implementation.

4 Methods

4.1 Synthesis

Commercially available starting materials 1-dodecylamine (97%, Alfa Aesar, CAS: 124-22-1), $MnCl_2 \cdot 4H_2O$ (98% Sigma-Aldrich, CAS: 13446-34-9), $MnBr_2 \cdot 4H_2O$ (98% Sigma-Aldrich, CAS: 10031-20-6), HBr (48% Thermo Scientific, CAS: 10035-10-6) and HCl (37% Thermo Scientific, CAS: 7647-01-0) were directly used for these studies. First, $[C_{12}H_{25}NH_3]X$ was prepared. For this purpose, 1-dodecylamine was dissolved in anhydrous alcohol and placed into an ice bath. The respective concentrated acid was added dropwise to the solution under stirring. The acid is added in a slight excess because it volatilizes during the acid–base reaction. $[C_{12}H_{25}NH_3]X$ is isolated and dried by rotary evaporation and dried in a vacuum. Then, $[C_{12}H_{25}NH_3]_2MnX_4$ was prepared through a stoichiometric reaction between $[C_{12}H_{25}NH_3]X$ and $MnX_2 \cdot 4H_2O$ in anhydrous ethyl alcohol, and the solution was evaporated under reduced pressure to obtain a white crystalline powder.

To prepare PDMS composites with a conductive additive (AC), a commercial Sylgard 184 kit (Sigma-Aldrich), which includes a silicone base and a curing agent, is used. These components are mixed in a 10 : 1 mass ratio (2 grams of silicone base to 0.2 grams of curing agent) and manually homogenized. After achieving a uniform blend, specific amounts of $[C_{12}H_{25}NH_3]_2MnCl_4$ and graphite are added to the mixture to create the corresponding composites. The mixture becomes colored and more viscous due to the polymerization reaction.

The blended mixture is then poured into a homemade 3D printed mold made of polylactic acid (PLA) filament with circular holes 15 mm in diameter and 4 mm in height. The mixture is left to cure for 72 hours until it solidifies into pellets.

For the 3D printed composites, a commercial Elegoo Mars 4 Ultra 3D printer was used with commercial F39 white flexible rubber-like resin (Resione). To enhance thermal conductivity, a ~16% (w/w) concentration of barocaloric material and a 5.5% (w/w) concentration of graphite powders were added to the resin, and then moved into an automatic stirrer until all components were integrated. The printing parameters of exposure time, bottom exposure time, and layer height were 250 seconds, 550 seconds and 0.090 mm, respectively, to produce pellets with a diameter of 13 mm and a height of 5 mm.

4.2 Powder X-ray diffraction (PXRD)

The obtained materials were characterized by powder X-ray diffraction (PXRD) using a Siemens D-5000 diffractometer with Cu(Kα) radiation at room temperature. The obtained patterns were compared with those simulated from reported single-crystal XRD.[12]

The structural evolution of the material at different temperatures and pressures was studied by synchrotron powder X-ray diffraction (SPXRD) using a wavelength of $\lambda = 0.60172$ Å. These studies were carried out at the BM01 Swiss Norwegian Beamline (SNBL) of the European Synchrotron Radiation Facility (ESRF).[72] For the VT-SPXRD experiments, 0.5 mm diameter quartz capillaries were filled with powder and measured *in situ* at atmospheric pressure, and the temperature was controlled with an Oxford Cryostream 700+. For the VP-SPXRD experiments, 1.0 mm diameter sapphire capillaries were filled with a powder mixture with silicone oil and measured *in situ* at variable pressure (up to 900 bar) applied by silicone oil and the temperature was controlled with an Oxford Cryostream 700+.[73]

The diffraction data were collected with a Pilatus 2 M detector. The recorded 2D patterns were integrated into a 1D powder profile and fitted using the Le Bail method. The diffraction patterns were refined using the GSAS-II software.[74]

4.3 Scanning electron microscopy (SEM)

The homogeneity and distribution of $[C_{12}H_{25}NH_3]_2MnCl_4$ in the different PDMS and F39 3D printed composites were analyzed using a JEOL JSM-7200F Schottky field-emission scanning electron microscope (FE-SEM). Chemical analyses were carried out using a JEOL JSM-7200F equipped with an Oxford Instruments X-Max detector for energy-dispersive X-ray spectroscopy (EDS).

4.4 Dynamic mechanical analysis

The strain–stress curves of the different materials ($[C_{12}H_{25}NH_3]_2MnCl_4$, PDMS, F39 3D printing resin, and selected composites) were measured using a Rheometric Scientific DMTA IV instrument at room temperature. For that purpose, geometrically identical pellets with a diameter of 1.3 cm and a thickness of 0.5 cm were chosen.

4.5 Stability studies

Samples of $[C_{12}H_{25}NH_3]_2MnCl_4$, a 3D printed composite of F39 with ~16% (w/w) of $[C_{12}H_{25}NH_3]_2MnCl_4$ and ~5.5% (w/w) of graphite powder, and a composite of PDMS with ~19% (w/w) of $[C_{12}H_{25}NH_3]_2MnCl_4$ and ~7% (w/w) of graphite powder were placed in ethylene glycol at room temperature with magnetic stirring for 3 days. The enthalpy changes of the as-synthesized materials and after 3 days of treatment were measured using differential scanning calorimetry. A Teledyne Isco 65D pressure pump fed with nitrogen gas was used for mechanical stability tests of 3D printed gyroid-like composites. For that purpose, gyroid fragments were selected and tested for over 100 pressurization cycles under isothermal conditions of 66 °C (above the phase transition) at a rate of 115 bar min^{-1} from 200 to 1000 bar – across the phase transition (see Fig. S13). Thermal stability analysis was performed using a TGA-DTA Thermal Analysis SDT2960 instrument, where 15 mg of pure barocaloric material and 3D printed composite pellets were heated at a rate of 5 °C min^{-1} from room temperature to 650 °C, using an alumina crucible and under a flow of dry nitrogen.

4.6 Differential scanning calorimetry

Preliminary analysis on variable-temperature differential scanning calorimetry at ambient pressure was performed on

a Setaram DSC Setline instrument using ~4 mg of the different samples in a temperature range from 310 to 360 K with a heating rate of 20 K min^{-1}.

Quasi-direct and direct barocaloric methods were performed using variable-pressure differential scanning calorimetry (VP-DSC) on a mDSC7 EVO microcalorimeter equipped with a Teledyne Isco 65D pressure pump that utilized nitrogen gas as the pressure-transmitting medium. Samples of ~20 mg of the different materials and composites were measured at 1 K min^{-1} rate, from 310 to 360 K at different isobaric pressures from atmospheric pressure and up to 1000 bar.

The calorimeter was previously calibrated according to the manufacturer's recommendations.

The thermal changes were calculated by integrating the heat flow, as reported elsewhere,[16] taking into account the calibrations described above, following eqn (2):

$$|\Delta S|_{0\rightarrow p} = \frac{1}{T}|\Delta H|_{0\rightarrow p} = \frac{1}{T}\int_0^p \left(\frac{dQ}{dp}\right) dp \quad (2)$$

where (dQ/dp) is the heat flow curve as a function of pressure, 0 and p are the initial and final pressures, and T is the temperature at each isothermal measurement.

Using this equipment, repeatability studies over time were performed in 3D printed pellet composites for over 100 pressurization cycles under isothermal conditions of 66 °C (above the phase transition) at a rate of 40 bar min^{-1} from 200 to 1000 bar – across the phase transition (see Fig. S12), while continuously registering heat flow.

Measurements of variable-temperature specific heat capacity (C_p) for the calculation of adiabatic temperature changes were performed using a TA Instruments Q2000 DSC calorimeter. For this purpose, ~4 mg of the different samples (pure $[C_{12}H_{25}NH_3]_2MnCl_4$ and 3D printed composite of F39 with ~16% (w/w) of $[C_{12}H_{25}NH_3]_2MnCl_4$) were measured in a temperature range of 310 to 360 K.

4.7 Thermal conductivity

The thermal conductivity was evaluated under ambient conditions using a C-Term Trident thermal conductivity analyser equipped with a 6 mm flexible transient plane source (TPS) sensor.

4.8 Heat exchange simulations

Heat exchange simulations were performed using COMSOL Multiphysics® software,[75] modelling cubic and gyroid structures for the pure $[C_{12}H_{25}NH_3]_2MnCl_4$ material and for the 3D printed composite, respectively. The simulated materials were defined by using the specific heat capacity, density and thermal conductivity of both the $[C_{12}H_{25}NH_3]_2MnCl_4$ material and the 3D printed composite, as obtained in this work.

The heat transfer and laminar flow modules were used to simulate both fluid flow and heat transfer. Additionally, the non-isothermal flow multiphysics interface was employed.

In the case of thermal management using ethylene glycol flow, a laminar flow regime was assumed with an inlet fluid velocity of 0.1 m s^{-1}, resulting in a Reynolds number below 1200, which is defined following the literature[76] as:

$$\mathrm{Re} = \frac{\rho u L_c}{\mu} \quad (3)$$

where ρ is the fluid density, u is the fluid velocity, L_c is the characteristic length, and μ is the dynamic viscosity of the fluid.

The mesh type used was physics-controlled with a finer element size to ensure adequate precision. As the mesh size decreases, the computational cost increases. In the case of thermal management by natural convection, the air volume walls were set as open boundaries, allowing constant airflow.

The governing mathematical equations used in the simulations are based on:

$$\frac{\partial \rho}{\partial t} + \nabla\cdot(\rho u) = 0 \quad (4)$$

$$\rho\frac{\partial u}{\partial t} + \rho(u\cdot\nabla)u = \nabla\cdot[-pI + \tau] + F + \rho g \quad (5)$$

$$\rho C_p\frac{\partial T}{\partial t} + \rho C_p u\cdot\nabla T\cdot\nabla\cdot q = Q \quad (6)$$

$$q = -k\nabla T \quad (7)$$

where p is the pressure, T is the temperature, τ is the viscous stress tensor, F is the volume force vector, C_p is the specific heat capacity, k is the heat conductivity in solid, q is the external heat flux and Q is the heat sources.

Author contributions

I. D.-F. and A. M.-F. contributed equally to this work and were involved in most of the experimental work. M. S.-A. and J. M. B.-G. conceived the project. I. D. F., J. G.-B., R. J. C. D., A. E. P., M. S. A. and J. M. B.-G. were involved in HP-DSC analysis. R. J. C. D., A. E. P., J. W., C. J. M. and M. G. were involved in VT-XRD analysis. J. L. B. and R. A. performed low-pressure DSC and C_p calculations. A. M.-F., S. C.-G., S. Z. M. A. S.-R. and J. M. B.-G. were involved in composites development, characterization and thermal studies, and outlook. D. G.-N. and A. B. performed heat transfer calculations. All authors were involved in the discussion of results and in the manuscript writing and revision. J. M. B.-G. directed and supervised this project.

Conflicts of interest

The authors declare no competing interests.

Data availability

The data supporting this article have been included as part of the supplementary information (SI). Supplementary information: additional crystallographic, microstructural, thermal and stability data. See DOI: https://doi.org/10.1039/d5ta04364f.

Acknowledgements

The authors acknowledge financial support from the project PID2021-122532OB-I00 funded by MCIU/AEI/10.13039/501100011033/and by U-ERDF and from the projects ED431C 2022/39 and ED431F 2023/33 funded by Xunta de Galicia. This publication is part of the grant RYC2021-033040-I, funded by MCIU/AEI/10.13039/501100011033 and the European Union « NextGenerationEU»/PRTR», and was granted to J. M. B.-G. This researcher is also grateful for the support received from UDC-Inditex InTalent Programme. This work was supported by the Engineering and Physical Sciences Research Council, UK [grant number EP/S03577X/1]. J. G.-B. and M. G. acknowledge Xunta de Galicia for Postdoctoral (ED481B/2024) and Predoctoral (ED481A/2023) Fellowships, respectively. The authors thank ESRF for the award of beam time (A01-2-1291 on BM01). I. D.-F. thanks the Spanish Ministry of Science, Innovation and Universities for a FPU fellowship. The Table of Contents (TOC) graphical abstract was created in BioRender. Bermúdez, J. (2025) **https://BioRender.com/fcyrbdt**. Funding for open access charge: Universidade da Coruña/CISUG.

References

1 International Energy Agency, *Net Zero by 2050 A Roadmap for the Global Energy Sector*, 2021.
2 S. G. Nnabuife, E. Oko, B. Kuang, A. Bello, A. P. Onwualu, S. Oyagha and J. Whidborne, *Sustain. Chem. Clim. Action*, 2023, **2**, 100024.
3 A. Faghri and Z. Guo, *Int. J. Heat Mass Transf.*, 2005, **48**, 3891–3920.
4 J. Xu, C. Zhang, Z. Wan, X. Chen, S. H. Chan and Z. Tu, *Renew. Sustain. Energy Rev.*, 2022, **155**, 111908.
5 X. Zhang, Z. Li, L. Luo, Y. Fan and Z. Du, *Energy*, 2022, **238**, 121652.
6 S. Shahid and M. Agelin-Chaab, *Energy Convers. Manag. X*, 2022, **16**, 100310.
7 N. De Miguel, B. Acosta, D. Baraldi, R. Melideo, R. Ortiz Cebolla and P. Moretto, *Int. J. Hydrogen Energy*, 2016, **41**, 8606–8615.
8 M. M. Lee, J. Teuscher, T. Miyasaka, T. N. Murakami and H. J. Snaith, *Science*, 2012, **338**, 643–647.
9 J. Burschka, N. Pellet, S.-J. Moon, R. Humphry-Baker, P. Gao, M. K. Nazeeruddin and M. Grätzel, *Nature*, 2013, **499**, 316.
10 L. Mao, C. C. Stoumpos and M. G. Kanatzidis, *J. Am. Chem. Soc.*, 2019, **141**, 1171–1190.
11 V. Busico, C. Carfagna, V. Salerno, M. Vacatello and F. Fittipaldi, *Sol. Energy*, 1980, **24**, 575–579.
12 R. Salgado-Pizarro, C. Puigjaner, J. García, A. I. Fernández and C. Barreneche, *J. Mater. Chem. A*, 2024, **12**, 18544–18553.
13 J. Li, M. Barrio, D. J. Dunstan, R. Dixey, X. Lou, J. L. Tamarit, A. E. Phillips and P. Lloveras, *Adv. Funct. Mater.*, 2021, **31**, 2105154.
14 J. Seo, R. D. McGillicuddy, A. H. Slavney, S. Zhang, R. Ukani, A. A. Yakovenko, S. L. Zheng and J. A. Mason, *Nat. Commun.*, 2022, **13**, 2536.
15 Y. Gao, H. Liu, F. Hu, H. Song, H. Zhang, J. Hao, X. Liu, Z. Yu, F. Shen, Y. Wang, H. Zhou, B. Wang, Z. Tian, Y. Lin, C. Zhang, Z. Yin, J. Wang, Y. Chen, Y. Li, Y. Song, Y. Shi, T. Zhao, J. Sun, Q. Huang and B. Shen, *NPG Asia Mater.*, 2022, **14**, 34.
16 *Barocaloric Effects in the Solid State: Materials and Methods*, ed. P. Lloveras, IOP Publishing, London, First., 2023.
17 Z. Zhang, K. Li, S. Lin, R. Song, D. Yu, Y. Wang, J. Wang, S. Kawaguchi, Z. Zhang, C. Yu, X. Li, J. Chen, L. He, R. Mole, B. Yuan, Q. Ren, K. Qian, Z. Cai, J. Yu, M. Wang, C. Zhao, X. Tong, Z. Zhang and B. Li, *Sci. Adv.*, 2023, **9**, 1–10.
18 C. Yu, J. Huang, J. Qi, P. Liu, D. Li, T. Yang, Z. Zhang and B. Li, *APL Mater.*, 2022, **10**, 011109.
19 P. Lloveras, E. Stern-Taulats, M. Barrio, J. L. Tamarit, S. Crossley, W. Li, V. Pomjakushin, A. Planes, L. Mañosa, N. D. Mathur and X. Moya, *Nat. Commun.*, 2015, **6**, 8801.
20 Q. Ren, J. Qi, D. Yu, Z. Zhang, R. Song, W. Song, B. Yuan, T. Wang, W. Ren, Z. Zhang, X. Tong and B. Li, *Nat. Commun.*, 2022, **13**, 1–9.
21 M. V Gorev, E. V Bogdanov, I. N. Flerov, A. G. Kocharova and N. M. Laptash, *Phys. Solid State*, 2010, **52**, 167–175.
22 M. V. Gorev, E. V. Bogdanov, I. N. Flerov, V. N. Voronov and N. M. Laptash, *Ferroelectrics*, 2010, **397**, 76–80.
23 I. N. Flerov, A. V. Kartashev, M. V. Gorev, E. V. Bogdanov, S. V. Mel'Nikova, M. S. Molokeev, E. I. Pogoreltsev and N. M. Laptash, *J. Fluorine Chem.*, 2016, **183**, 1–9.
24 M. V. Gorev, E. A. Mikhaleva, I. N. Flerov and E. V. Bogdanov, *J. Alloys Compd.*, 2019, **806**, 1047–1051.
25 Z. Zhang, X. Jiang, T. Hattori, X. Xu, M. Li, C. Yu, Z. Zhang, D. Yu, R. Mole, S. I. Yano, J. Chen, L. He, C. W. Wang, H. Wang, B. Li and Z. Zhang, *Mater. Horizons*, 2023, **10**, 977–982.
26 X. Xu, F. Li, C. Niu and H. Wang, *Appl. Phys. Lett.*, 2023, **122**, 043901.
27 P. Lloveras, A. Aznar, M. Barrio, P. Negrier, C. Popescu, A. Planes, L. Mañosa, E. Stern-Taulats, A. Avramenko, N. D. Mathur, X. Moya and J. L. Tamarit, *Nat. Commun.*, 2019, **10**, 1–7.
28 A. Aznar, P. Lloveras, M. Barrio, P. Negrier, A. Planes, L. Mañosa, N. Mathur, X. Moya and J. L. Tamarit, *J. Mater. Chem. A*, 2020, **8**, 639–647.
29 J. Li, D. Dunstan, X. Lou, A. Planes, L. Mañosa, M. Barrio, J.-L. Tamarit and P. Lloveras, *J. Mater. Chem. A*, 2020, **8**, 20354–20362.
30 A. Aznar, P. Negrier, A. Planes, L. Mañosa, E. Stern-Taulats, X. Moya, M. Barrio, J.-L. Tamarit and P. Lloveras, *Appl. Mater. Today*, 2021, **23**, 101023.
31 A. Salvatori, P. Negrier, A. Aznar, M. Barrio, J. L. Tamarit and P. Lloveras, *APL Mater.*, 2022, **10**, 111117.
32 K. Zhang, R. Song, J. Qi, Z. Zhang, Z. Zhang, C. Yu, K. Li, Z. Zhang and B. Li, *Adv. Funct. Mater.*, 2022, **32**, 2112622.
33 F. B. Li, M. Li, X. Xu, Z. C. Yang, H. Xu, C. K. Jia, K. Li, J. He, B. Li and H. Wang, *Nat. Commun.*, 2020, **11**, 1–8.
34 F. Li, C. Niu, X. Xu, M. Li and H. Wang, *Appl. Phys. Lett.*, 2022, **121**, 223902.
35 J. García-Ben, J. M. Bermúdez-García, R. J. C. Dixey, I. Delgado-Ferreiro, A. L. Llamas-Saiz, J. López-Beceiro,

R. Artiaga, A. Garcia-Fernandez, U. B. Cappel, B. Alonso, S. Castro-Garcia, A. E. Phillips, M. Sánchez-Andújar and M. A. Señarís-Rodríguez, *J. Mater. Chem. A*, 2023, **11**, 22232–22247.

36 W. Imamura, É. O. Usuda, L. S. Paixao, N. M. Bom, A. M. Gomes and A. M. G. Carvalho, *Chinese J. Polym. Sci.*, 2020, **38**, 999–1005.

37 S. Patel, A. Chauhan, R. Vaish and P. Thomas, *Appl. Phys. Lett.*, 2016, **108**, 1–5.

38 A. M. G. Carvalho, W. Imamura, E. O. Usuda and N. M. Bom, *Eur. Polym. J.*, 2018, **99**, 212–221.

39 A. Aznar, P. Lloveras, M. Romanini, M. Barrio, J.-L. Tamarit, C. Cazorla, D. Errandonea, N. D. Mathur, A. Planes, X. Moya and L. Mañosa, *Nat. Commun.*, 2017, **8**, 1851.

40 J. Min, A. K. Sagotra and C. Cazorla, *Phys. Rev. Mater.*, 2020, **4**, 1–10.

41 M. Romanini, Y. Wang, G. Kübra, G. Ornelas, P. Lloveras, Y. Zhang, W. Zheng, M. Barrio, A. Aznar, A. Gràcia-Condal, B. Emre, O. Atakol, C. Popescu, H. Zhang, Y. Long, L. Balicas, J. L. Tamarit, A. Planes, M. Shatruk and L. Mañosa, *Adv. Mater.*, 2021, **33**, 2008076.

42 S. P. Vallone, A. N. Tantillo, A. M. Santos, J. J. Molaison, R. Kulmaczewski, A. Chapoy, P. Ahmadi, M. A. Halcrow and K. G. Sandeman, *Adv. Mater.*, 2019, **31**, 1–7.

43 P. J. Von Ranke, B. P. Alho, P. H. S. Silva, R. M. Ribas, E. P. Nobrega, V. S. R. De Sousa, M. V Colaço, L. F. Marques, M. S. Reis, F. M. Scaldini, L. B. L. Escobar and P. O. Ribeiro, *J. Appl. Phys.*, 2020, **127**, 1–6.

44 J. Seo, J. D. Braun, V. M. Dev and J. A. Mason, *J. Am. Chem. Soc.*, 2022, **144**, 6493–6503.

45 P. J. Von Ranke, B. P. Alho, R. M. Ribas, E. P. Nobrega, A. Caldas, V. S. R. De Sousa, M. V. Colaço, L. F. Marques, D. L. Rocco and P. O. Ribeiro, *Phys. Rev. B*, 2018, **98**, 2–6.

46 P. J. Von Ranke, B. P. Alho and P. O. Ribeiro, *J. Alloys Compd.*, 2018, **749**, 556–560.

47 P. J. Von Ranke, B. P. Alho, E. P. Nobrega, A. Caldas, V. S. R. de Sousa, M. V. Colaço, L. F. Marques, G. M. Rocha, D. L. Rocco and P. O. Ribeiro, *J. Magn. Magn. Mater.*, 2019, **489**, 165421.

48 J. M. Bermúdez-García, M. Sánchez-Andújar, S. Castro-García, J. López-Beceiro, R. Artiaga and M. A. Señarís-Rodríguez, *Nat. Commun.*, 2017, **8**, 15715.

49 J. M. Bermúdez-García, S. Yáñez-Vilar, A. García-Fernández, M. Sánchez-Andújar, S. Castro-García, J. López-Beceiro, R. Artiaga, M. Dilshad, X. Moya and M. A. Señarís-Rodríguez, *J. Mater. Chem. C*, 2018, **6**, 9867–9874.

50 M. Szafrański, W. J. Wei, Z. M. Wang, W. Li and A. Katrusiak, *APL Mater.*, 2018, **6**, 100701.

51 J. Salgado-Beceiro, A. Nonato, R. X. Silva, A. García-Fernández, M. Sánchez-Andújar, S. Castro-García, E. Stern-Taulats, M. A. Señarís-Rodríguez, X. Moya and J. M. Bermúdez-García, *Mater. Adv.*, 2020, **1**, 3167–3170.

52 J. Salgado-Beceiro, J. M. Bermúdez-García, E. Stern-Taulats, J. García-Ben, M. Castro-García, S. Sánchez-Andújar, X. Moya and M. A. Señarís-Rodríguez, *ChemRxiv*, 2021, preprint, DOI: 10.33774/chemrxiv-2021-c4hx5.

53 J. García-Ben, J. López-Beceiro, R. Artiaga, J. Salgado-Beceiro, I. Delgado-Ferreiro, Y. V. Kolen'ko, S. Castro-García, M. A. Señarís-Rodríguez, M. Sánchez-Andújar and J. M. Bermúdez-García, *Chem. Mater.*, 2022, **34**, 3323–3332.

54 M. Gelpi, J. García-Ben, S. Rodríguez-Hermida, J. López-Beceiro, R. Artiaga, Á. Baaliña, M. Romero-Gómez, J. Romero-Gómez, S. Zaragoza, J. Salgado-Beceiro, J. Walker, C. J. McMonagle, S. Castro-García, M. Sánchez-Andújar, M. A. Señarís-Rodríguez and J. M. Bermúdez-García, *Adv. Mater.*, 2024, **36**, 2310499.

55 Henry Royce Institute, *Materials for the Energy Transition Roadmap: Caloric Energy Conversion Materials*, 2020.

56 P. Lloveras and J.-L. Tamarit, *MRS Energy Sustain.*, 2021, **8**, 3–15.

57 Y. Liu, H. Zhou, Z. Xu, D. Liu, J. Li, F. Hu and T. Ma, *Mater. Res. Lett.*, 2022, **10**, 675–681.

58 W. Imamura, E. O. Usuda, É. S. N. Lopes and A. M. G. Carvalho, *J. Mater. Sci.*, 2022, **57**, 311–323.

59 R. Salgado-Pizarro, A. Svobodova-Sedlackova, A. I. Fernández and C. Barreneche, *J. Energy Storage*, 2023, **73**, 109156.

60 K. Wu, W. Cui and J. Zhang, *Thermochim. Acta*, 2007, **463**, 15–17.

61 K. Wu, J. Zhang and X. Liu, *Thermochim. Acta*, 2009, **483**, 55–57.

62 M. Bochalya, G. V. Prakash and S. Kumar, *J. Solid State Chem.*, 2019, **273**, 32–36.

63 L. Guo, Y. Sun, A. Mei, Y. Dai and H. Liu, *J. Wuhan Univ. Technol. Mater. Sci. Ed.*, 2008, **23**, 490–494.

64 L. Zhu, Z. Dai, Y. Gao, D. Wu, C. Wang, D. Zhao, X. She, Y. Ding and X. Zhang, *J. Therm. Sci.*, 2023, **32**, 2115–2125.

65 Y. H. Gao, D. H. Wang, F. X. Hu, Q. Z. Huang, Y. T. Song, S. K. Yuan, Z. Y. Tian, B. J. Wang, Z. B. Yu, H. B. Zhou, Y. Kan, Y. Lin, J. Wang, Y. L. Li, Y. Liu, Y. Z. Chen, J. R. Sun, T. Y. Zhao and B. G. Shen, *Nat. Commun.*, 2024, **15**, 1–13.

66 FEBUS, *A Success Story of Fuel Cell Buses Deployment*, 2022.

67 Y. Ye, J. Lu, J. Ding, W. Wang and J. Yan, *Appl. Energy*, 2020, **278**, 115682.

68 Y. Ye, J. Ding, W. Wang and J. Yan, *Appl. Energy*, 2021, **299**, 117255.

69 D. Erdemir and I. Dincer, *Appl. Therm. Eng.*, 2023, **219**, 119524.

70 T. T. Nikolaos Chalkiadakis, A. Stubos, E. Stamatakis, E. Zoulias, in *Hydrogen Electrical Vehicles*, Wiley, 2023.

71 N. Weerasekera, H. Jiang, Y. Chen, G. Sumanasekera and B. Bhatia, *Energy Technol.*, 2025, **13**, 1–10.

72 V. Dyadkin, P. Pattison, V. Dmitriev and D. Chernyshov, *J. Synchrotron Radiat.*, 2016, **23**, 825–829.

73 C. J. McMonagle, D. R. Allan, M. R. Warren, K. V. Kamenev, G. F. Turner and S. A. Moggach, *J. Appl. Crystallogr.*, 2020, **53**, 1519–1523.

74 B. H. Toby and R. B. Von Dreele, *J. Appl. Crystallogr.*, 2013, **46**, 544–549.

75 *COMSOL Multiphysics® v.6.3.*, COMSOL AB, Stockholm, Sweden, https://www.comsol.com/.

76 M. Chen, Y. Shi, L. Yang, C. Yan, B. Song, Y. Liu, Z. Dou and Y. Chen, *Case Stud. Therm. Eng.*, 2024, **61**, 105095.